

# Nonlinear dynamics at the interface of two-layer stratified flows over pronounced obstacles.

Cecilia Cabeza, Juan Varela, Italo Bove, Daniel Freire, Arturo C. Martí, and L. G. Sarasúa  
*Instituto de Física, Universidad de la República, Montevideo, Uruguay*

Gabriel Usera  
*Instituto de Mecánica de los Fluidos, Facultad de Ingeniería,  
 Universidad de la República, Montevideo, Uruguay*

Raul Montagne\* and Moacyr Araujo  
*Laboratório de Oceanografia Física Estuarina e Costeira, Departamento de Oceanografia,  
 Universidade Federal de Pernambuco, 50740-550, Recife, PE, Brazil*  
 (Dated: October 27, 2018)

The flow of a two-layer stratified fluid over an abrupt topographic obstacle, simulating relevant situations in oceanographic problems, is investigated numerically and experimentally in a simplified two-dimensional situation. Experimental results and numerical simulations are presented at low Froude numbers in a two-layer stratified flow and for two abrupt obstacles, semi-cylindrical and prismatic. We find four different regimes of the flow immediately past the obstacles: sub-critical (I), internal hydraulic jump (II), Kelvin-Helmholtz at the interface (III) and shedding of billows (IV). The critical condition for delimiting the experiments is obtained using the hydraulic theory. Moreover, the dependence of the critical Froude number on the geometry of the obstacle are investigated. The transition from regime III to regime IV is explained with a theoretical stability analysis. The results from the stability analysis are confirmed with the DPIV measurements. In regime (IV), when the velocity upstream is large enough, we find that Kelvin-Helmholtz instability of the jet produces shedding of billows. Important differences with flows like Von Karman's street are explained. Remarkable agreement between the experimental results and numerical simulations are obtained.

PACS numbers: 47.55.Hd, 47.20.Ft

## I. INTRODUCTION

The interaction between topography and flows with density interfaces is of interest both for fundamental reasons and for its relevance to practical problems. A most challenging problem is to describe and quantify the characteristic features occurring at the interface of a stratified flow passing over an obstacle. The interaction between stable stratified flows and obstacles is a widespread phenomenon in nature. In the atmosphere, for example, the flow around buildings or mountains is particularly important because such conditions are often associated with high levels of atmospheric pollution due to low wind speeds and suppressed vertical mixing [1, 2]. In physical oceanography, the interaction of marine currents with topographic features, such as ocean banks and coastlines, results in a complex system of circulation [2, 3, 4, 5, 6, 7]. In this case, observational, analytical, numerical, and previous laboratory studies [8, 9, 10, 11, 12, 13, 14, 15, 16, 17, 18, 19, 20, 21, 22, 23, 24] suggest that the combination of streamlines splitting, current intensification, and breaking of internal lee waves, play a significant role as a mixing source in the ocean [25]. Also, seamounts

have a decisive impact on enhancing the biological productivity and acting over the ecological processes that determine the structure of local ocean life [26, 27]. The rich diversity of geo-biophysical scenarios entirely justify the efforts for understanding the physics of the local instability at the density interface, along with the conditions for which the generated lee waves break down.

Among the topographic effects on flows a particular problem that has received considerable amount of attention is the oceanic observations in the Knight Inlet, a fjord in central British Columbia, Canada. The Knight Inlet experiment provided field observations of tidal flow over a large sill [4]. This work led to a series of papers reporting different issues and possible explanation of them [28, 29, 30, 31]. This fjord has a strong tidal flow which generates internal waves propagating along a pycnocline on both sides of a sill there. Farmer and Armi [4] have observed that a very large lee wave is formed behind the sill, while a train of strong depression pulses are generated on the upstream side.

Efforts has been dedicated to the upstream generation of solitary waves [20, 21, 30, 32] and also on the trapped wedge of mixed fluid behind the sill. Upstream influence as a consequence of variable forcing, has been widely discussed in theoretical analysis, laboratory experiments and numerical simulations of stratified flow [28, 33]. Flow separation by a topographic obstacle and the final stage of vortex shedding has also received attention [28, 29, 34].

---

\*Present Address: Departamento de Física Universidade Federal Rural de Pernambuco 52171-900, Recife, PE, Brasil

Model simulations of the lee wave formation by Lamb [31] exhibit a stable flow over the sill until the lee wave overturns. All those work agree that the larger-scale response can be sensitively dependent on small-scale instabilities. In the present work we focus on small-scale instabilities, addressing an analysis on the different regimes that appear downstream flow, near the obstacle. The importance of the geometry of the obstacle in the transition from subcritical to supercritical will be demonstrated. Finally, we prove the Kelvin–Helmholtz (KH) instability at the two layers interface, is the triggering mechanism for the vortex shredding.

Under suitable conditions, mainstream ceases to flow approximately parallel to the obstacle beyond a certain point (as the flow in a divergent channel) causing the phenomenon of separation [31, 35]. In these cases, the flow next to the wall usually reverses its direction in some regions. Analytic theories for lee waves and hydraulic jumps usually assume that flow separation does not occur [1]. However, when the topography is abrupt, that is, the vertical component of the velocity can not be neglected, flow separation is expected. Thus, in the present paper we compare experimental and numerical results with those obtained from hydraulic theories in the case of abrupt obstacles.

The interaction between stratified flows and topography has been also investigated by means of laboratory experiments. In Ref. [16] the lee-wave breaking process which occurs at low Froude numbers has been studied in the case of a strong linear stratification and two-dimensional smooth (Gaussian-shaped) obstacles. In a slightly different setup, the structure of the far-wake vortices generated by a moving sphere in a linearly stratified medium was investigated in Ref. [12]. In this work the authors suggest that these vortices exhibit universal features similar to large-scale vortices found in the ocean. The case in which both stratification and rotation are important has been study in Refs. [13, 14], where the role of laboratory experiments performed in close relation with numerical simulations is emphasized.

In our previous work [36] we studied numerically and experimentally the different instabilities developed in a two-layer stratified flow over a pronounced obstacle. The existence of a concentrated jet in the lee side of the obstacle was demonstrated and we showed that the Kelvin–Helmholtz (KH) instability at the interface constitutes a more efficient source of mixing between the two-layers than the internal hydraulic jump. Here, we extend our work to two-layer flows over prismatic and semi-cylindrical abrupt obstacles focusing on the role of the geometry, the appearance of secondary instabilities after KH, and the shedding of billows.

The experiments were performed in a way that the flow could be assumed bidimensional. We use two layers of different density, with constant density inside each layer. We look for different regimes of the flow past the obstacles. The experimental results, obtained via direct visualization and also with Digital Particle Image Velocime-

try (DPIV), showed to be in qualitative good agreement with numerical simulations and theoretical results. Four different regimes were found, depending on the global Froude number  $F_0$  and aspect ratio  $H_m$ . A complete diagram in the parameter space was obtained. The transition from the regime III to IV was explained with a stability analysis of the jet past the obstacle. Those analytical results were validated by velocity measurements with DPIV technique.

This paper is organized as follows. In Section II we briefly review the treatment of two-layer flows using hydraulic theory. In Section III we present the experimental setup. The numerical simulations are given in Sec. IV. The results obtained from the experiments and simulations and their comparison are given in Sec. V. In Section VI we present the results of linear stability analysis, which are relevant for the flow past the obstacle. Finally, a summary and the conclusions are given in section VII.

## II. HYDRAULIC THEORY OF A TWO-LAYER FLOW PROBLEM

Let us consider a linear theory for a flow consisting of two layers of different densities  $\rho_1$  and  $\rho_2$  ( $\rho_2 > \rho_1$ ) over a fixed obstacle. Through this paper the subindexes 1 and 2 correspond respectively to the upper and lower layer. We define a Cartesian reference frame with coordinates  $(x, y, z)$ , where the flow is in the  $x$  direction and  $z$  is directed vertically upwards. As we mentioned in the introduction, we shall focus on the situations where variations in the  $y$  direction can be neglected and the problem can be considered bi-dimensional. The depths of the layers are functions of  $x$ , as the thickness of them depends on the position where it is measured. Thus, the depth of the upper and lower layers are  $d_1(x)$  and  $d_2(x)$ , respectively, and the height of the obstacle is  $h(x)$  as sketched in figure 1. Far upstream the depths are named  $d_1(x=0) = d_{10}$  and  $d_2(x=0) = d_{20}$ .

The mean velocities of the fluid in each layer are  $u_1$  and  $u_2$ . Let us assume that the fluid velocity is uniform far upstream, with  $u_{10} = u_{20} = U$ . In addition, we assume: a) the pressure is hydrostatic, b) the Boussinesq approximation, which implies that  $\epsilon = (\rho_2 - \rho_1)/\rho_2 \ll 1$ , is valid, and c) the top boundary of the upper layer is a free surface at constant pressure  $p_s$ , taken to be  $p_s = 0$ . The flow over the topography is then characterized by the densities  $\rho_1, \rho_2$ , the depth of the layers  $d_1, d_2$ , the mean velocity in each layer  $u_1, u_2$  and the height of the obstacle  $h$ . With these assumptions, the Bernoulli functions for each layer may be written as:

$$\begin{aligned} E_1 &= \rho_1 g(d_2 + d_1 + h) + \frac{1}{2} \rho_1 u_1^2 \\ E_2 &= \rho_1 g d_1 + \rho_2 g(d_2 + h) + \frac{1}{2} \rho_2 u_2^2 \end{aligned} \quad (1)$$

Following Lawrence's model [37, 38], from the conditions  $dE_i/dx = 0$  and imposing mass conservation in each

layer the following relation is obtained

$$\frac{(1 - F^2)}{\epsilon F_1^2 F_2^2} \frac{dD}{dx} = \frac{dh}{dx} \quad (2)$$

where  $F^2 = F_1^2 + F_2^2 - \epsilon F_1^2 F_2^2$  is the composite internal Froude number while  $F_i^2 = u_i^2/(g'd_i)$  ( $i = 1, 2$ ) are the Froude numbers for each layer with  $g' = (1 - \frac{\rho_1}{\rho_2})g$ , and  $D = d_1 + d_2 + h$ . It has been shown [37] that  $F$  is the adequate composite Froude number for characterizing a two-layer flow; i.e. if  $F > 1$  the flow is internally supercritical (the internal small waves cannot propagate upstream against the background flow), and if  $F < 1$  the flow is subcritical (the disturbances may propagate in both directions). When  $F = 1$ , the flow is termed critical and this location is usually called a control point. The transition from subcritical to supercritical flow is of special interest in our experiment. When the flow is supercritical, internal hydraulic jump may take place which is an important source of turbulence and mixing. From Eq. (2), it follows that the critical condition  $F = 1$ , may occur if  $dh/dx = 0$ . For that value of  $F$  the flow under goes a transition from subcritical to supercritical when the surface has horizontal tangent, i.e. at the crest of the obstacle. If, in addition, the condition  $\epsilon \ll 1$  is imposed (which is satisfied in our experiments), the composite Froude number may be expressed as  $F^2 = F_1^2 + F_2^2$ . On the other hand, in the present study we consider flows where  $F_i^2 \lesssim 1$ . Thus, from Eq. (2) and the Boussinesq approximation it follows that

$$\frac{dD}{dx} = \frac{\epsilon F_1^2 F_2^2}{1 - F^2} \frac{dh}{dx} \approx 0, \quad (3)$$

therefore we consider  $D = d_{10} + d_{20}$  a constant. Hence the free surface will be taken as horizontal.

In order to obtain the critical values of the flow parameters for the subcritical-supercritical transition, we impose that  $E_2 - E_1$  is constant and using the Boussinesq approximation, then

$$\frac{1}{2}r(1-r)F_0^2 \left( \frac{r_0^2}{r^2} - \frac{(1-r_0)^2}{(1-r_0H-r)^2} \right) + r_0(H-1) + r = 0 \quad (4)$$

where  $r = d_2/D$ ,  $r_0 = d_{20}/D$ ,  $H = h/d_{20}$  and

$$F_0 = \sqrt{\frac{U^2}{g'd_{10}} + \frac{U^2}{g'd_{20}}} \quad (5)$$

is the Froude number  $F$  calculated in the upstream flow far from the obstacle. We shall call  $F_0$  as the global Froude number. On the other hand, the critical condition  $F^2 = 1$  may be expressed as

$$r(1-r)F_0^2 \left( \frac{r_0^2}{r^3} + \frac{(1-r_0)^2}{(1-r_0H-r)^3} \right) - 1 = 0. \quad (6)$$

Thus, Eqs. (4) and (6), imposed at the crest of the

obstacle, may be used to determine,  $F_{0c}$ , the critical value of  $F_0$  for the occurrence of supercritical flow. In our experiments we fixed the aspect ratio  $r_0 = 0.6$ , and we considered different values of  $H_m = h_m/d_{20}$ ,  $h_m$  being the height of the obstacle. The critical values,  $F_{0c}$ , for the occurrence of critical flows as a function of  $H_m$  are obtained solving equations (4) and (6). The results are shown in Sec. V, Fig. 7, where are compared with the experimental results.

Theoretical solutions for the flow when  $F_0$  is larger than  $F_{0c}$ , i.e. when the flow is beyond the critical condition, have been obtained in Refs.[1, 38]. These solutions predict that there is range of values of  $F_0$  for which there is a wave that moves backwards to the flow changing the conditions upstream. These approaches allow the calculation of the velocity and amplitude of this wave. This kind of wave has been also obtained using the KdV equation [39], and numerical simulations, with step like stratification [32] and linearly varying stratification [21]. This effect may difficult the experiments inside the container in some cases. However, we show that quantitative good results may be obtained within a broad range of parameter values.

### III. EXPERIMENTAL SETUP

Our experiments were performed in a water tank of size equal to  $2.0 \times 0.29 \times 0.137$  m<sup>3</sup>. We used a closed channel where we towed the obstacle at different velocities with a calibrated motor (Fig. 2). The velocities of the fluid were calculated in a reference frame fixed to the obstacle. In our previous work [36], we showed that this configuration is equivalent to the flow over a fixed obstacle. Moreover, we focused our observations only on the central region of the tank where the structures are persistent and the far boundaries effects can be neglected. In this work, we always show images and diagrams of leftward moving obstacles. We used two different obstacle shapes, prismatic and semi-cylindrical, both of them having a height of  $h_m = 0.125$  m, width  $W_0 = 0.13$  m and length of  $L = 0.25$  m, see Fig. 3. The obstacles were scaled in such a way that the confinement aspect ratio verifies  $W_0/W \lesssim 1$  ( $W = 0.137$  m, width of the water tank) and the lateral flow around the obstacle can be neglected in order to reduce the problem to a quasi-two dimensional situation. As mentioned above, we want to model a density profile with an abrupt gradient at the interface. In order to get this step-like stratification we first filled the tank with a layer of density  $\rho_2 = 1002$  kg/m<sup>3</sup> using NaCl solution. To fill the upper layer, pure water with density  $\rho_1 = 1000$  kg/m<sup>3</sup> was carefully poured over a sponge floating on the free surface. The time scale of the molecular diffusion between the layers is much longer than the typical experimental times. Despite that, due to the mixing produced by the moving obstacle, after a few measurements, the tank had to be emptied and new fluid layers poured again.

The flow was examined via two standard techniques: dye visualization and digital particle image velocimetry (DPIV). In the first case, the upper layer was dyed with a  $\text{KMnO}_4$  solution in order to obtain a good visual contrast between both layers. A powerful source of fluorescent light from behind was used to obtain a uniform illumination. We obtained global qualitative picture of the flow with this technique. In the second case, DPIV allows us to obtain quantitative values of velocity field based on the cross-correlation of two consecutive images recorded by a digital camera. Neutrally buoyant polyamide particles of  $50 \times 10^{-6} \text{ m}$  diameter were seeded in the bottom layer. A green laser sheet of 100 mW is used to illuminate a cross section plane of the flow which is recorded by a digital camera PIXELINK PL-A741. In order to control the interface and avoid attenuation of the LASER light as much as possible, when using this technique, only a thin layer of water at the bottom of the upper layer is dyed. For both obstacle shapes, five different sets of heights were chosen, always keeping constant the characteristic ratio  $r_0 = 0.6$ . The experiment was repeated for each set of heights with a wide range of velocities analyzing the different behaviors, using the two mentioned visualization techniques.

#### IV. NUMERICAL METHOD

The numerical simulations considered here were obtained with the in-house flow solver *caffa3d.MB* [40] developed jointly by Universitat Rovira i Virgili (Tarragona, Spain) and Universidad de la República (Montevideo, Uruguay). It is an original Fortran95 implementation of a fully implicit finite volume method for solving the 3D incompressible Navier-Stokes equations in complex geometry using block structured grids. This three-dimensional solver, based on a previous two-dimensional solver [41], is described and validated in [42, 43].

The unsteady incompressible Navier-Stokes equations with Boussinesq approximation for buoyancy terms were considered. Since the Reynolds number was below  $\text{Re}=8.10^2$  for all cases, no turbulence model was required, thus transient solutions were computed directly. The time step was set to  $2.0 \times 10^{-2} \text{ s}$  for all cases. This time scale is about  $(h_m/U)/10^3$  for the highest velocity case. Simulations were run starting from null velocity fields through  $10^4$  time steps, or about 200 s of flow time.

In the simulations, the obstacle remains fixed against a steady two-layer current of fluid. Thus a uniform velocity profile was specified at the upstream boundary located at a distance of  $8h_m$  upstream from the obstacle, and a null gradient outlet was used at the downstream boundary, located  $15h_m$  downstream. As the top surface is not disturbed by the flow, it was modeled as an horizontal slip boundary at fixed height. All other boundaries correspond to wall surfaces and non-slip condition was directly applied to them, including the vertical walls of the channel. Thus, the simulation accounts fully for

three-dimensional effects, although the flow reveals itself as essentially two dimensional owing to the geometry of the obstacles and the relatively low Reynolds numbers.

For both obstacles the grid was made up of three blocks, although the topology was different in each case. For the prismatic obstacle three straight blocks were assembled, two at each side of the obstacle and the third extending on top of them along the domain. On the other hand, for the cylindrical obstacle one C-grid block was used around the obstacle together with two other straight blocks, upstream and downstream of the obstacle.

Grid resolution was set essentially uniform through the domain at  $h_m/25$ , being enough to resolve flow details at these rather low Reynolds numbers. Due to the layout of the grid in the cylindrical obstacle case the spatial resolution normal to the wall was slightly higher near the obstacle, reaching about  $h_m/35$ .

#### V. RESULTS

In this section we are going to discuss the experimental and numerical results, which exhibit a great qualitative agreement between them. It is also worth noting that, in spite of quantitative differences, the results for both topographic shapes show a qualitative similarity. Let us start discussing the different regimes observed in the experiments. Using the dye technique we visualized the different regimes as a function of the obstacle velocity and the aspect ratio. In Fig. 4 (Fig. 5), we show experimental and numerical results for the prismatic (semi-cylindrical) obstacle. The aspect ratio and the height of the bottom layer are the same for both obstacles, i.e.  $r_0 = 0.6$  and  $d_{20} = 15 \text{ cm}$ .

In these figures we distinguish four regimes, all of them present in both obstacles. However, both, experimental and numerical results reveals one very important point: the regimes take place at different critical Froude number for different geometries. For the prismatic obstacle, the velocities vary between 0.12 cm/s ( $F_0 = 0.035$ ) and 0.64 cm/s ( $F_0 = 0.187$ ). While for the semi-cylindrical obstacle, the velocities vary between 0.13 cm/s ( $F_0 = 0.039$ ) and 0.43 cm/s ( $F_0 = 0.125$ ). The numerical simulation for both obstacles were performed at the same global Froude numbers as the experimental results.

All the different behaviors of the downstream flow correspond to the case in which the flow upstream is subcritical, i.e.  $F_0 < 1$ . The thickness of the layers varies from one point to another immediately after the obstacle, as can be seen in Figs. 4 and 5, and consequently the Froude number  $F$  too. We look for the first critical value of the local Froude number ( $F = 1$ ), over the obstacle in a place where  $d_2$  is minimal and where the velocity is higher.

The regime (I) corresponds to the situations in which the flow is subcritical,  $F < 1$ , along all the flow over the obstacle. At low velocity, we observe that a jet through

the bottom layer is flowing near the obstacle. As the velocity is increased, the jet begins to separate from the obstacle and rise towards the horizontal.

A transition from regime (I) to (II) occurs when Froude number reaches a control point ( $F = 1$ ) somewhere over the obstacle. In regime (II) the flow is subcritical upstream, and supercritical past the obstacle. As a consequence, an internal hydraulic transition is developed at the lee side. The interface between the layers is smoothly disturbed both in regime (I) and (II), however, over the obstacle the interface is stable enough not to break but to induce a jet in the lower layer. When the velocity gradient between the jet and the surrounding fluid is strong enough a Kelvin-Helmholtz instability appears inside the lower layer at the lee side of the obstacle. The wavelength of KH depends on two densities and the velocity profile (see Sec. VI). The regimes (II) and on, are all supercritical past the obstacle,  $F > 1$  beyond the critical point.

Further increasing the Froude number  $F_0$  (still below 1), we reach regime (III) where it is clearly visible a lee wave that perturbs the interface separating the two layers, with a quasi-sinusoidal profile. Downstream, a secondary instability develops and a kind of mixing is observed. Finally, the regime (IV) is characterized by the shedding of vortical portions of lighter fluid separated from the upper layer. As a consequence, intense mixing between the two layers takes place. In this regime, the interface between both layers is strongly disturbed. The jet drags fluid from the upper layer and billows formation appear. It is worth mentioning that the frequency of the shedding is almost constant with respect of variation in the velocity  $U$ .

The numerical results are in good agreement with the experimental results, as can be visualized in Figs. 4 and 5. The regimes observed in the experiments were also obtained in the numerical simulations for the two obstacles that we used. As  $F_0$  gets larger the behavior of the numerical and the experimental results differs. For the case of the prismatic obstacle the vortex shedding starts before than in the simulations (Fig. 4d). Whereas in the cylinder case the numerical experiments shows a vortex shedding before the experiments (Fig. 5 d). These differences will be explained further on. The overall agreement between numerical and experimental method is good as can be seen in Fig. 6 which compares numerical and experimental results corresponding to regime III and IV. The flow separation occurs before in the experiments for low  $F_0$  (Fig. 6 a-b). However for greater  $F_0$  the situation inverts (Fig. 6 c-d).

In Fig. (7) we show the global Froude number  $F_0$  as a function of the aspect ratio  $H_m$  for the transition from sub-critical to super-critical. The continuous line corresponds to the theoretical global Froude number for a smooth obstacle as it was calculated solving equations (4) and (6). The experimental  $F_0$  is represented with open squares for the semi-cylindrical obstacle and filled squares for the prismatic one. The dashed lines are the linear fitting of the experimental points. This graph

clearly reflects the fact that the smoother the obstacle, the higher the velocity that will be needed to reach the critical Froude number. Then, the critical values for the semi-cylindrical obstacle are aligned between the values of the prismatic obstacle and the smoother theoretical prediction. In this way, by means of the laboratory experiments we prove that the transition from one regime to another strongly depends on the geometry, the sub-critical flow may correspond to a supercritical flow for another geometry.

In order to obtain the transition between the different regimes, we use the DPIV technique. For the same parameters of the previous situation,  $d_{20} = 15$  cm and prismatic obstacle, we observed that when the velocity is lower than  $U = 0.11$  cm/s, we obtained a sub-critical flow. The transition between sub-critical to super-critical flow takes place at  $U = 0.12$  cm/s ( $F_0 = 0.035$ ). For  $U = 0.38$  cm/s ( $F_0 = 0.111$ ), KH instability at the interface appears. Finally, for velocities higher than  $U = 0.64$  cm/s ( $F_0 = 0.19$ ) shedding of billows takes place. Figure 8 summarizes in a stability diagram the different regimes as a function of the global Froude number  $F_0$  and the aspect ratio  $H_m$  for  $r_0 = 0.6$ . The diagram shows the transition values between the regimes for the prismatic (full symbols) and semi-cylindrical (open symbols) obstacles. The dotted lines are linear approximations. We show for  $H_m = 0.83$ , in open symbols the transitions between the different regimes for the cylindrical obstacle. It is interesting to note that, although the prismatic obstacle reaches the super critical regime at a lower velocity than the semi-cylindrical obstacle, KH develops at higher velocities than in the case of the semi-cylindrical obstacle.

The slope of the jet after the obstacle plays an important role in the transition between the different regimes. Indeed, it was observed that transition depends not only on  $F_0$ ,  $r_0$  and  $H_m$  but also in the shape of the obstacle, i. e. the slope of the jet after the obstacle. As a result, the lee waves past the prismatic and semi-cylindrical obstacles have similar characteristics at different Froude numbers. We exemplified this in figure 9. We show KH instability at the interface for the two obstacles. Despite the prismatic obstacle reaching the super critical regime at a lower velocity than the semi-cylindrical obstacle, the abrupt geometry of the bank makes difficult to rise up the jet and develop KH. Thus, for the prismatic obstacle, KH develops at higher velocities than in the case of the semi-cylindrical obstacle.

We characterized the velocity profile via DPIV analysis. Figure 10 (b) shows the visualization of the velocity profile over the semi-cylindrical obstacle obtained with DPIV technique at the places indicated in Fig. 10 (a). We observe that the shape of the jet is nearly triangular and quite constant at different distances from the obstacle. These facts will be used to make an hydraulic stability analysis of the interface (see Sec. VI).

In regime III as the flow velocity  $U$  is increased, the inclination of the jet, the amplitude of the interface wave

$U$ (cm/s)	$a$ (cm)	$x_b$ (cm)	$x_b/a$
0.45	2.1	5.4	2.6
0.55	2.3	6.2	2.7
0.65	2.8	7.4	2.6

TABLE I: Thickness of the jet  $a$  and distance between the billows  $x_b$  for  $r_0 = 0.6$  and  $H_m = 0.83$ .

and the velocity of the jet increase. However, when the Froude number exceeds the critical value, the wave at the interface is no longer observed and the flow enters in regime IV. In this regime, there is shedding of vortical portions of the more lighter fluid which submerge into the lower layer.

The shedding of billows in regimen (IV), as can be seen in figure 11, provide evidence that the instabilities which lead to this regimen could be caused by a KH instability. In order to test this hypothesis, we correlate the thickness of the jet  $a$  and the distance between the billows  $x_b$ . If the shedding was caused by KH instability, the distance between the billows must be approximately the wavelength of the most unstable mode. Table I shows the values of  $a$ ,  $x_b$  and the ratio between them for the case  $r_0 = 0.6$  and  $H_m = 0.83$ , for the prismatic obstacle at different velocities. These results reveals a clear proportionality between  $a$  and  $x_b$ , with a slope of  $x_b/a = 2.7$ . Indeed, in the next section we consider a triangular jet, and we show that the dimensionless wavenumber of the most unstable mode is given by  $kb = 1.225$ . Then, the ratio between the corresponding wavelength and the thickness of the jet  $a$  ( $a = 2b$ ) is given by  $\lambda/a = 2.57$ , which is in very good agreement with the ratio (2.6 – 2.7), obtained experimentally.

As commented in Sec. II theoretical solutions based on hydraulic theory predicts that for  $F_0 > F_{0c}$  there is a wave that propagates in opposite sense to the flow, modifying the upstream conditions. The role of this upstream wave has been profusely studied theoretical, observational and numerically [4, 28, 30, 31]. We address here, the question of how much this feature affects our results.

In order to study the effect of this upstream wave, we performed numerical simulations, in a broad range of values of the  $F_0$ , focusing on the dynamics far upstream the obstacle and looking for the transitory effects. The temporal evolution of the upstream wave, for  $F_0 = 0.35$ , is shown in Fig. 12. We note that the profile of the upstream wave is very smooth in comparison with the downstream perturbation. Accumulation of wave effects in the closed container for Froude numbers clearly exceeding the critical condition produces that the thickness of the layers are larger than those obtained in an unlimited flow. This effect is more important as larger the  $F_0$  is. For instance, from the theory [1] follows that for  $F_0 = 0.181$  and  $H_m = 0.833$ , the increment of the thickness is significant,  $d'_{10}/d_{10} = 1.10$ , where  $d'_{10}$  is the thickness of the

interface taking into account the effects of the upstream wave. On the other hand, for  $F_0 = 0.11$ ,  $d'_{10}/d_{10} = 1.03$ , this estimation shows that the effects of this wave are negligible. Furthermore we note that the results in Fig. 7 and Fig. 8 for  $F_0 < 0.11$  are not distorted in any way by the upstream effect. In the region  $F_0 > 0.11$  although the results could be slightly distorted, they remains qualitatively correct as we can conclude from comparison with the numerical simulations.

## VI. STABILITY ANALYSIS OF THE JET PAST THE OBSTACLE

### A. Kelvin-Helmholtz Instability

As described in section V, in the lee side of the obstacle the flow presents different regimes depending on the values of  $F_0$ ,  $r_0$  and  $H_m$ . However the type of flow downstream is not only determined by the flow parameters but also by the slope of the jet past the obstacle. We will analyze the stability of this flow.

In regime III, the interface between the two layers is perturbed by a quasi-sinusoidal wave, which breaks down when its amplitude is sufficiently large, indicating that a secondary instability takes place. The DPIV measurements clearly show that the jet is located near the interface, we conjecture that this wave results from a primary Kelvin-Helmholtz instability. We test this hypothesis based in the experimental measures shown in Fig. 10 (b) and we will describe the flow near the interface as a triangular jet. The flow is given by

$$V = \begin{cases} V_1 & \text{for } z > b \text{ and } z < -b, \\ V_2 + (V_1 - V_2)|z|/b & \text{for } -b < z < b, \end{cases} \quad (7)$$

where  $2b$  is the thickness of the jet and the densities are  $\rho_2$  for  $z < b$  and  $\rho_1$  for  $z > b$ . We perform standard linear stability analysis assuming a stream function of the perturbations  $\psi$  of the form [44]

$$\psi(x, z, t) = \phi(z) \exp(ik(x - ct)), \quad (8)$$

where  $\exp(ik(x - ct)) = \exp(ik(x - c_r t)) \exp \sigma t$ , with  $\sigma = kc_i$ , and  $c_i, c_r$  are the imaginary and real parts of the phase velocity  $c$ . Thus,  $\sigma$  represents the growing rate of the perturbations. If  $\sigma > 0$ , then the flow is unstable to these perturbations, and if  $\sigma < 0$  the flow is stable. Since the flow under consideration has constant density in each layer,  $\phi(z)$  is determined by Rayleigh's equation:

$$\phi''(z) - k^2 \phi(z) = 0, \quad (9)$$

whose general solution is  $\psi_i(z) = A_i \exp(kz) + B_i \exp(-kz)$ , where the index  $i = 1, 2, 3, 4$  denotes the solution for the regions  $z > b$ ,  $b > z > 0$ ,  $0 > z > -b$  and  $z < -b$  respectively. The perturbations must be bounded

at  $z \rightarrow \infty$  and  $z \rightarrow -\infty$ , then the  $\phi_i$ 's become

$$\begin{aligned}\phi_1(z) &= B_1 \exp(-kz) \\ \phi_2(z) &= A_2 \exp(kz) + B_2 \exp(-kz) \\ \phi_3(z) &= A_3 \exp(kz) + B_3 \exp(-kz) \\ \phi_4(z) &= A_4 \exp(kz).\end{aligned}\quad (10)$$

We now impose the boundary conditions across the limits separating the regions by requiring continuity of vertical velocity and pressure. Since the velocity profile is continuous, the first of these conditions is equivalent to require  $\phi_i(z_j) = \phi_{i+1}(z_j)$  [44], where  $z_j$  denotes the position of the boundary that separates regions  $i$  and  $i + 1$ . The second of these conditions requires

$$(U_i(z_j) - c)\phi'_i(z_j) - U'_i(z_j)\phi_i = (U_{i+1}(z_j) - c)\phi'_{i+1}(z_j) - U'_{i+1}(z_j)\phi_{i+1}.$$

The boundary condition yield a linear system of equation on  $(B_1, A_2, B_2, A_3, B_3, A_4)$ . The dispersion relation, i. e. the relationship between  $k$  and  $c$ , is obtained banishing the trivial solution. The numerical results obtained by solving the dispersion relation are shown in figure (13). The normal mode stability analysis yields that the more unstable mode corresponds to the wavenumber  $k = 1.225/b$ . For  $b = 1.1$  cm (see Fig. 10 b), the corresponding wavelength is  $\lambda = 10.3$  cm which is in good agreement with the experimental data of  $\lambda = 10.2$  cm. We also performed the linear stability analysis of a jet that is located near the wall of the obstacle, with field velocity given by

$$V = \begin{cases} V_1 & \text{for } z \geq b, \\ V_2 + (V_1 - V_2)|z|/b & \text{for } -b < z < b, \end{cases} \quad (11)$$

where the rigid boundary is located at  $z = -b$ , and the densities are  $\rho_2$  for  $z < b$  and  $\rho_1$  for  $z > b$ . In this case, we have three regions with corresponding stream functions  $\phi_1(z), \phi_2(z), \phi_3(z)$ . The condition at the rigid boundary is given by  $\phi_3(-b) = 0$  [44], and the other boundary conditions are the same as the ones imposed for the unbounded jet. From this analysis we obtained that the jet is partially stabilized in the proximity of the wall of the obstacle, that is, the instabilities grow slowly compared with the unbounded case (Fig. (13)). This result is in agreement with those obtained previously by Hazel [45]. This stabilizing effect is caused by the combination of the density stratification and the presence of the wall. Then the wall has little effect on the stability of the jet, if the density is constant. This explains why the instabilities appear downstream, but not over the obstacle, where the jet is located on a rigid boundary.

The stability analysis results and the measured wavelength of the lee waves in the regimes III and IV, strengthen the assumption that the instabilities observed past the obstacle in both cases are caused by Kelvin-Helmholtz instability. We can also explain the fact that the frequency of the billows is almost independent of the velocity  $U$ . From Table I we can see that the thickness of

the jet is (for fixed  $r_0$  and  $H_m$ ) practically proportional to  $U$ . The frequency of the billows can be expressed as  $f = x_b/u_b$ , where  $u_b$  is the velocity of the billows. Since  $x_b$  is nearly proportional to  $U$ , if we assume that  $u_b$  is proportional to  $U$ , then the frequency is weakly dependent on the velocity  $U$ . This is in contrast with vortices produced in flows like the Von Karman's street, where the frequency, in a wide velocity range, is almost proportional to the velocity. The difference resides in the fact that in the Von Karman's flow, the characteristic length is constant (the diameter of the cylinder), while here the characteristic length (the thickness of the jet) varies almost proportional with  $U$ , which causes that the wavelength of the most dangerous mode increases with  $U$ . This effect compensates the increasing of  $u_b$  with  $U$ , leaving the frequency almost constant.

## VII. SUMMARY AND CONCLUSIONS

In this work, we studied two-layer stratified flow over abrupt obstacles, more specifically prismatic and semi-cylindrical. It is remarkable that in all cases, the critical value of the global Froude number,  $F_0$ , is less than that predicted by the hydraulic theory. In those cases, the vertical components of the velocity over the obstacles cannot be neglected. As a consequence of its smoother geometry, the results for the semi-cylindrical obstacle are closer to the hydraulic theory than those of the prismatic one. This result indicates that an abrupt obstacle reaches the control point for lower velocities than for a smooth obstacle. In other words, for a given  $F_0$ , a flow subcritical for a geometry could be supercritical for another geometry. Despite the fact of being approximate, the hydraulic theory allow us to estimate the thickness and averaged velocity of the strong jet that forms past the obstacle. However the presence of flow separation and dissipation at the lee side of the obstacle prevent the use of hydraulic theory for making further predictions.

For the downstream flow, four different regimes were identified and represented in the parameter space  $F_0 - H_m$ . We showed typical images of them in Fig. 4. In all the regimes observed the flow upstream remains subcritical. In regime I, the flow is subcritical everywhere, i.e. upstream and downstream. In regime II and all the subsequent regimes the flow past the obstacle is supercritical. The regime II is characterized by the transition from subcritical to supercritical by the local Froude number experimentally measured. Also in regime II, a shear instability develop mainly in the lower layer. The interface that separates the layers is disturbed with a quasi-sinusoidal wave in regime III. This disturbance is due to Kelvin-Helmholtz instability. Furthermore, this quasi-sinusoidal wave disturbance breaks down through a secondary instability for sufficiently large amplitude and departure from two-dimensionality takes place. Regime IV is characterized by the shedding of billows. This process increases the rate of mixing between the two layers.

A stability analysis on the jet immediately after the obstacle allowed us to verify that the shedding was also produced by Kelvin-Helmholtz instability. The characteristic length of the most dangerous mode of the stratified jet is in agreement with the distance between the billows. We have also shown that the stabilizing effect resulting from the combination of the proximity to an rigid boundary and stratification turns out in not observing any instabilities over the obstacle.

We studied the wave that propagates upstream when  $F_0 > F_{0c}$ . In the simulations, we reproduced this wave with excellent agreement with the hydraulic theory. The enhancement of the deeper layer thickness as well as the velocity of the fluid inside it are in very good agreement with the theory [1]. These results indicate that the effect of this wave must be considered in flows exceeding the critical conditions. For  $F_0$  of the order 0.1 or less, the effects of the wave may be negligible. Furthermore, the results in Fig. 7 and Fig. 8 for  $F_0 < 0.1$  are not distorted in any way by the upstream effect. For this region of the space diagram, and high enough  $H_m$ , there are still the four different regimes, as it was described before and also in this region vortex shedding takes place. In the region  $F_0 > 0.10$  the results remains qualitatively correct as we

can conclude from the numerical results comparison.

The experimental and simulation results showed that the inclination of the jet plays a central role. Immediately after the separation, as velocity  $U$  increases the inclination of the jet decreases. However, when  $U$  is larger than a critical value, the inclination of the jet increases as the velocity  $U$  increases. When the flow enters in regime IV, the jet slope is pronounced. The different regimes reported in this work appeared for both obstacles, but, since separation is a phenomenon strongly dependent on the curvature of the surface, the critical values for passing from one regime to another depend on the geometry of the obstacle.

### VIII. ACKNOWLEDGMENTS

We acknowledge financial support from PEDECIBA (PNUD URU/06/004, Uruguay), Latin American Center for Physics (CLAF) and Grants PDT54/037. R. M. acknowledge financial support from the Brazilian agencies, CNPq, FAPERN, FACEPE.

- 
- [1] P. G. Baines, *Topographic Effects in Stratified Flows*, Cambridge University Press, Cambridge, 1995.
  - [2] J.F. Scinocca and W.R. Peltier, "Pulsating downslope windstorm," *J. Atmos. Scien.* **46**, 2885 (1989).
  - [3] J.A. Carrillo, M.A. Sanchez, A. Platonov, and J.M. Redondo, "Coastal and interfacial mixing. Laboratory experiments and satellite observations," *Phys. Chem. Earth B* **26**, 305 (2001).
  - [4] D.M. Farmer and L. Armi, "Stratified flow over topography: the role of small-scale entrainment and mixing in flow establishment," *Phil. Trans. R. Soc. Lond. A* **455**, 3221 (1999).
  - [5] J.M. Klymak and M.C. Gregg, "Tidally generated turbulence over the Knight inlet sill," *J. Phys. Ocean.* **34**, 1135 (2004).
  - [6] J.N. Moum and J.D. Nash, "Topographically induced drag and mixing at a small bank on the continental shelf," *J. Phys. Ocean.* **30**, 2049 (2000).
  - [7] C.R. Torres, A.S. Mascarenhas Jr., and J.E. Castillo, "Three-dimensional stratified flow over Alarcón Seamount, Gulf of California entrance," *Deep-Sea Research* **11**, 647 (2004).
  - [8] D. Apsley and I. Castro, "Numerical computation of stratified flow over obstacles," in *Mixing in Geophysical Flows, International Center for Numerical Methods in Engineering*, edited by J. M. Redondo and O. Metais, p. 87, Barcelona, Spain, 1995.
  - [9] L. Armi and D.M. Farmer, "Maximal two-layer exchange through a contraction with a barotropic net flow," *J. Fluid Mech.* **164**, 27 (1986).
  - [10] P. Baines, "A unified description of two-layer flow over topography," *J. Fluid Mech.* **146**, 127 (1984).
  - [11] P.G. Baines and J.A. Whitehead, "On multiple states in single-layer flows," *Phys. Fluids* **15**, 298 (2003).
  - [12] M. Bonnier, O. Eiff, and P. Bonneton, "On the density structure of far-wake vortices in a stratified fluid," *Dyn. Atmos. Ocean* **31**, 117 (2000).
  - [13] D. Boyer and P. Davies, "Laboratory studies of orographic effects in rotating and stratified flows," *Ann. Rev. Fluid Mech.* **32**, 165 (2000).
  - [14] D. Boyer, P. Davies, W. Holland, F. Biolley, and H. Honji, "Stratified rotating flow over and around isolated three-dimensional topography," *Phil. Trans. R. Soc. Lond. A* **322**, 213 (1987).
  - [15] R. Dewey, D. Richmond, and C. Garrett, "Stratified tidal flow over a bump," *J. Phys. Ocen.* **35**, 1911 (2005).
  - [16] O. S. Eiff and P. Bonneton, "Lee-wave breaking over obstacles in stratified flow," *Phys. Fluids* **12**, 1073 (2000).
  - [17] D.M. Farmer and L. Armi, "Maximal two-layer exchange over a sill and through the combination of a sill and contraction with a barotropic net flow," *J. Fluid Mech.* **164**, 53 (1986).
  - [18] M. Jamali, B. Seymour, and R. Kasaiian, "Numerical and experimental study of flow of a stratified fluid over a sill towards a sink," *Phys. Fluids* **17**, 057106 (2005).
  - [19] G. Pawlak and L. Armi, "Vortex dynamics in a spatially accelerating shear layer," *J. Fluid Mech.* **376**, 1 (1998).
  - [20] M. Stastna and W.R. Peltier, "Upstream-propagating solitary waves and forced internal-wave breaking in stratified flow over a sill," *Proc. R. Soc. Lond. A* **460**, 3159 (2004).
  - [21] M. Stastna and W. Peltier, "On the resonant generation of large-amplitude internal solitary and solitary-like waves," *J. Fluid Mech.* **543**, 267 (2005).
  - [22] G. Taylor, "Motion of solids in fluids when the flow is not irrotational," *Phil. Trans. R. Soc. Lond. A* **93**, 99 (1947).



- [23] P. Travassos, F. Hazin, J. Zagaglia, R. Advíncula, and J. Schober, “Thermohaline structure around seamounts and islands off North–Eastern Brazil,” *Arch. Fish. Mar. Res.* **47**, 211 (1999).
- [24] J. Verron and C. LeProvost, “A numerical study of quasigeostrophic flow over isolated topography,” *J. Fluid Mech.* **154**, 231 (1985).
- [25] G.N. Ivey, K.B. Winters, and J.R. Koseff, “Density stratification, turbulence, but how much mixing?” *Annu. Rev. Fluid Mech.* **40**, 169 (2008).
- [26] A. D. Rogers, “The biology of seamounts,” *Adv. Mar. Biol.* **30**, 305 (1994).
- [27] A. Genin, “Bio-physical coupling in the formation of zooplankton and fish aggregations over abrupt topographies,” *J. Mar. Sys.* **50**, 3 (2004).
- [28] P. F. Cummins, S. Vagle, L. Armi, and D.M. Farmer, “Stratified flow over topography: upstream influence and generation of nonlinear internal waves,” *Phil. Trans. R. Soc. Lond. A* **459**, 1467 (2003).
- [29] D.M. Farmer and L. Armi, “The generation and trapping of solitary waves over topography,” *Science* **283**, 188 (1999).
- [30] D.M. Farmer and L. Armi, “Stratified flow over topography: models versus observation,” *Proc. R. Soc. Lond. A* **457**, 2827 (2001).
- [31] K. G. Lamb, “On boundary-layer separation and internal wave generation at the Knight Inlet sill,” *Phil. Trans. R. Soc. Lond. A* **460**, 2305 (2004).
- [32] J. Grue, “Generation, propagation, and breaking of internal solitary waves,” *Chaos* **15**, 037110 (2005).
- [33] L. Armi and D.M. Farmer, “Stratified flow over topography: bifurcation fronts and transition to uncontrolled state,” *Phil. Trans. R. Soc. Lond. A* **458**, 513 (2002).
- [34] S. Vosper, I. Castro, W. Snyder, and S. Mobbs, “Experimental studies of strongly stratified flow past three-dimensional orography,” *J. Fluid Mech.* **390**, 223 (1999).
- [35] G. Batchelor, *An introduction to fluid dynamics*, Cambridge University, New York, eighth edition, 2007.
- [36] J. Varela, M. Aaujo, I. Bove, C. Cabeza, G. Usera, A. C. Martí, R. Montagne, and L. Sarasúa, “Instabilities developed in stratified flows over pronounced obstacles,” *Physica A* **386**, 681 (2007).
- [37] G. A. Lawrence, “On the hydraulics of boussinesq and non-boussinesq two-layer flows,” *J. Fluid Mech.* **215**, 457 (1990).
- [38] G. A. Lawrence, “The hydraulics of steady two-layer flow over a fixed obstacle,” *J. Fluid Mech.* **254**, 605 (1993).
- [39] W.K. Melville and K.R. Helfrich, “Transcritical two-layer flow over topography,” *J. Fluid Mech.* **178**, 31 (1987).
- [40] G. Usera, the code is freely available for academic use through the web site ([www.fing.edu.uy/imfia/caffa3d.MB](http://www.fing.edu.uy/imfia/caffa3d.MB)).
- [41] Z. Lilek, S. Muzaferija, M. Peric, and V. Seidl, “Computation of unsteady flows using non-matching blocks of structured grid,” *Numerical Heat Transfer. Part B, Fundamentals* **32**, 403 (1997).
- [42] G. Usera, A. Vernet, and J. Ferré, “Use of time resolved PIV for validating LES/DNS of the turbulent flow within a PCB enclosure model,” *Flow Turbulence Combust.* **77**, 77 (2006).
- [43] G. Usera, A. Vernet, and J. Ferré, “A parallel block-structured finite volume method for flows in complex geometry with sliding interfaces,” *Flow Turbulence Combust.* (in press), (2008).
- [44] P. Drazin and W. H. Reid, *Hydrodynamic Stability*, Cambridge University Press, Cambridge, second edition, 2004.
- [45] P. Hazel, “Numerical studies of the stability of inviscid stratified flows,” *J. Fluid Mech.* **51**, 39 (1972).

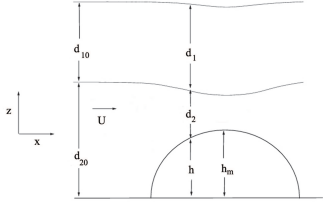


FIG. 1: Sketch showing variables used in the description of the two-layer flow.  $\vec{U}$  is the upstream uniform fluid velocity,  $d_1$ ,  $d_2$  are the depth of the layers and  $h$  is the height of the obstacle at a given location with  $h_m$  the maximum height of it.

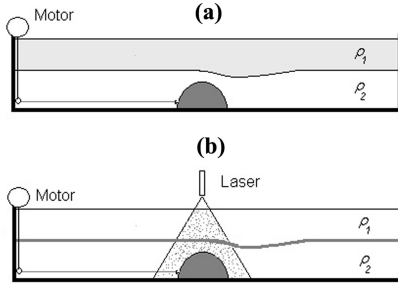


FIG. 2: Schematic diagram of the experimental configuration and the two visualization techniques used. a) The upper layer is dyed with  $\text{KMnO}_4$  to obtain good contrast for visualization when the tank is lighted from behind. b) The DPIV is carried out lightening from above with a LASER. In this case, in order to distinguish the interface, only a thin portion of the upper layer is dyed.

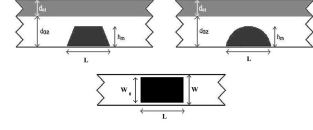


FIG. 3: Side (top) and plan view (bottom) of the prismatic and semi-cylindrical obstacles. Where  $d_{10}$ ,  $d_{20}$  are the depth of the layers,  $h_m$  the maximum height and  $L$  the length of the obstacle.  $W$  is the width of the water tank and  $W_0$  the width of the obstacle.

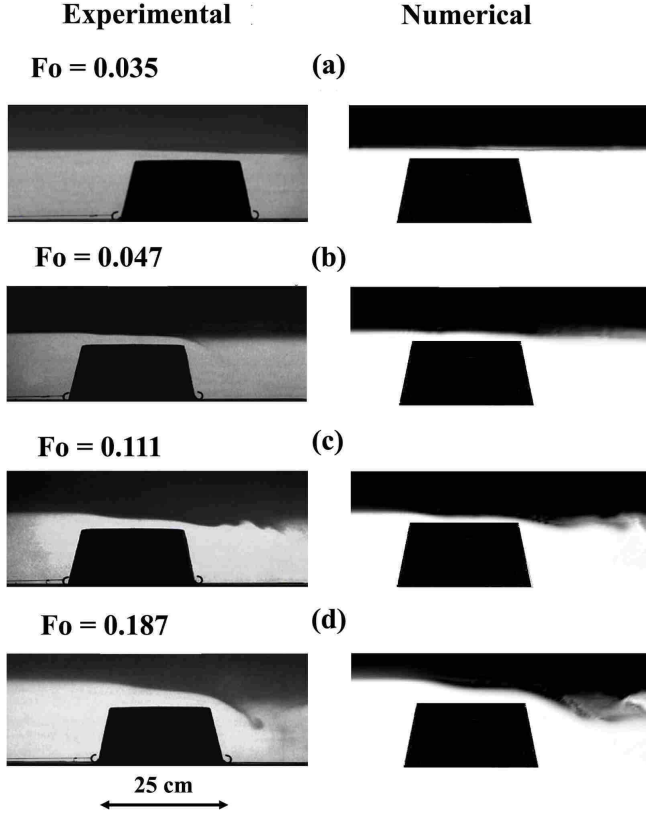


FIG. 4: Experimental snapshots (left) and numerical simulations of a flow (right) past an prismatic obstacle corresponding to  $d_{10} = 0.10$  m (upper layer),  $d_{20} = 0.15$  m (bottom layer) corresponding to the different regimes. a) Subcritical regime (I). b) Internal hydraulic transition (II). c) KH instability at the interface (III). d) Billow formation (IV). In all the images the aspect ratio is  $r_0 = 0.6$  and values of the the Froude numbers  $F_0$  are indicated.

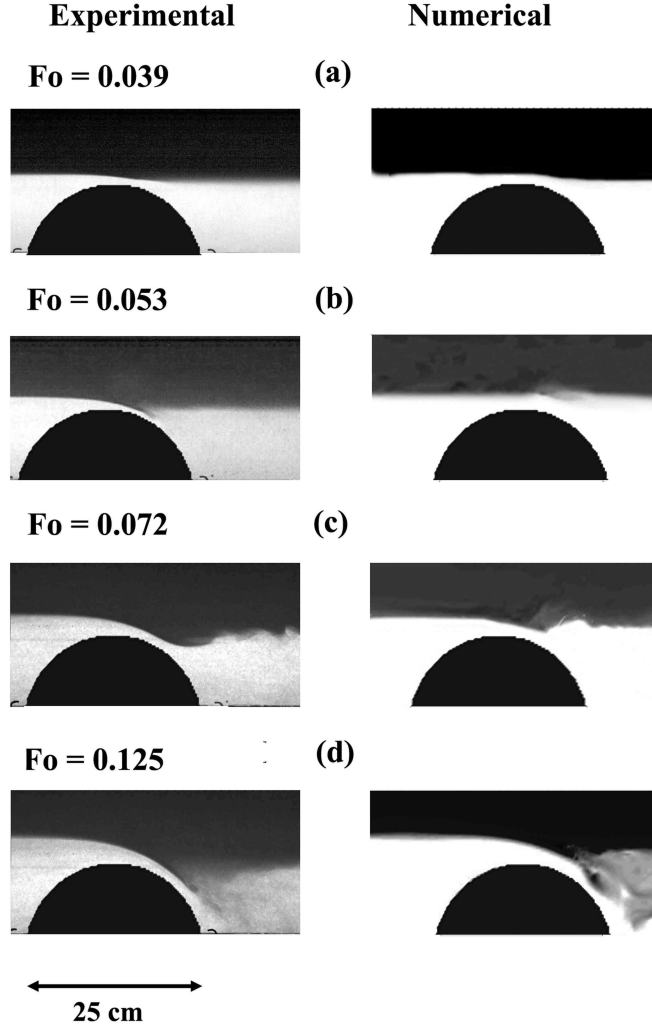


FIG. 5: Experimental snapshots (left) and numerical simulations of a flow (right) past an semi-cylindrical obstacle corresponding to  $d_{10} = 0.10$  m (upper layer),  $d_{20} = 0.15$  m (bottom layer) corresponding to the different regimes. a) Subcritical regime (I). b) Internal hydraulic transition (II). c) KH instability at the interface (III). d) Billow formation (IV). Same parameters as in Fig.4.

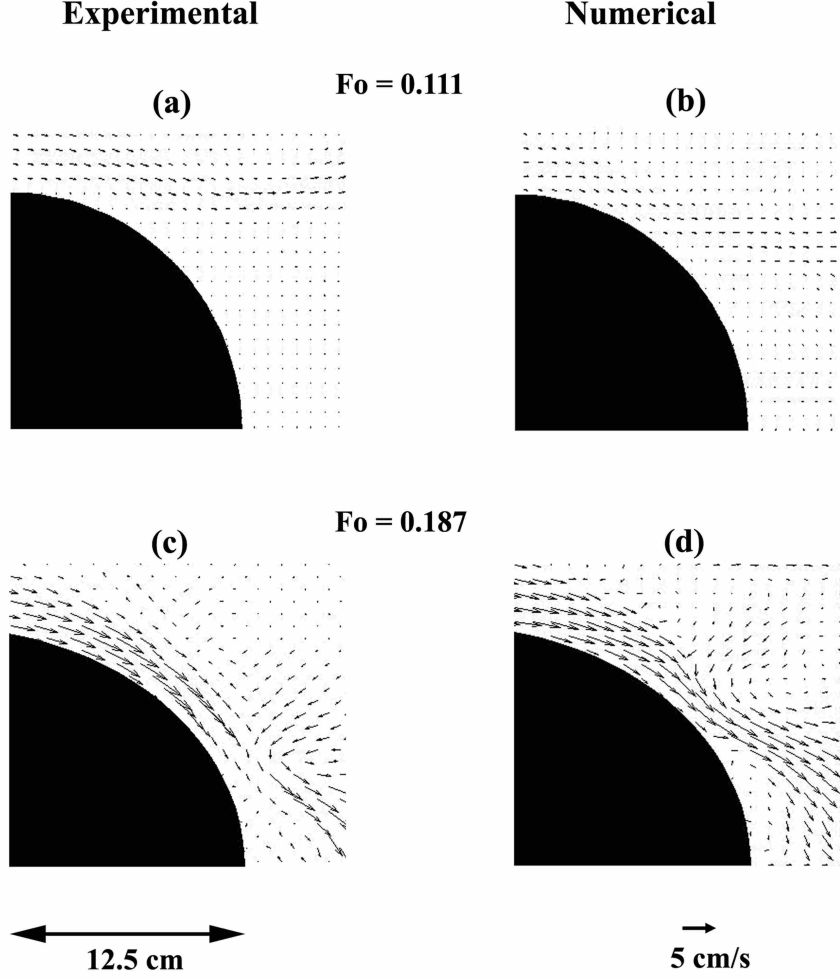


FIG. 6: Comparison between experimental (left) and numerical (right) results for semi-cylindrical obstacle. Top row  $d_{20} = 15$  cm and  $U = 0.38$  cm/s and  $F_0 = 0.111$ . Bottom row  $d_{20} = 15$  cm and  $U = 0.64$  cm/s and  $F_0 = 0.187$ .

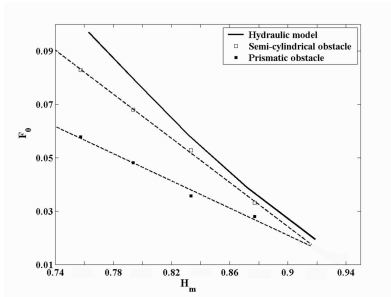


FIG. 7: Critical Global Froude number as a function of the aspect ratio  $H_m = h_m/d_{20}$ , for a fixed relation between the height of the layers  $r_0 = 0.6$ . The continuous line corresponds to the hydraulic model and the symbols to the experimental results of the two obstacles considered: semi-cylindrical (open squares) and prismatic (full squares).

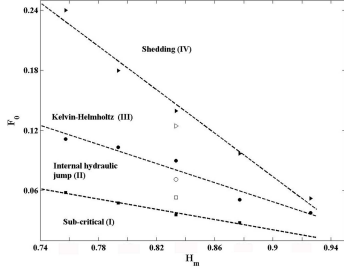


FIG. 8: Stability diagram of the different regimes for the prismatic and the semi-cylindrical obstacle as a function of the global Froude number  $F_0$  and the aspect ratio  $H_m = h_m/d_{20}$ . The relation between the height of the two layers is fixed to  $r_0 = 0.6$ . The full symbols correspond to the experimentally obtained transition between different regimes for the prismatic obstacle. Dotted lines are linear approximations of those experimental points. The open symbols correspond to the transition points for the semi-cylindrical obstacle for  $H_m = 0.83$ . Squares (full and open), correspond to the transition between sub-critical to internal hydraulic jump regimen. Circles (full and open), correspond to the onset of Kelvin-Helmholtz regimen. Triangle symbol (full and open), correspond to the shedding of billows regimen.

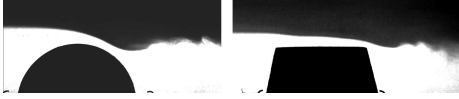


FIG. 9: Flow passing over the two obstacles of different geometry. These snapshots correspond to the Kelvin-Helmholtz instability between both layers at  $U = 0.35$  cm/s for the prismatic obstacle and at  $U = 0.22$  cm/s for the semi-cylindrical obstacle.

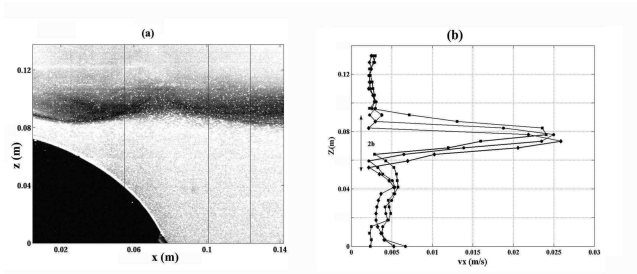


FIG. 10: a) DPIV image for the semi-cylindrical obstacle for KH instability at  $F_0 = 0.122$ . The vertical lines correspond to the places where the velocity profiles were taken. b) Velocity profiles for the three positions marked in the image displayed in a)

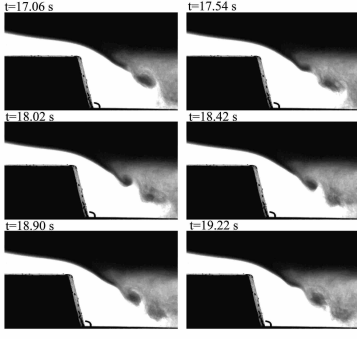


FIG. 11: Shedding of billows for  $H_m = h/d_2 = 0.76$ ,  $r_0 = 0.6$  and  $F = 0.26$  for the prismatic obstacle. The frequency of shedding is  $0.5 \text{ s}^{-1}$ .

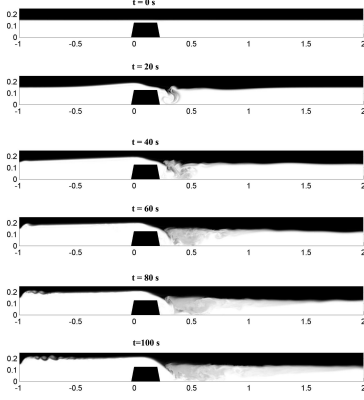


FIG. 12: Transient evolution of the interface showing the upstream influence of the wave corresponding to  $F_0 = 0.35$ . The simulations start at  $t = 0$  with a null-velocity condition.

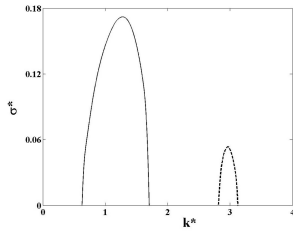


FIG. 13: Non-dimensional growing rate of the perturbations for the unbounded stratified jet (continuous line) and the stratified jet near a wall (dashed line), defined by Eqs.(7) and (11), where  $k^* = kb$  and  $\sigma^* = \sigma b/(V_2 - V_1)$ .